JOURNAL OF GEOPHYSICAL RESEARCH, VOL. 95, NO. C1, PAGES 761–773, JANUARY 15, 1990

Wind Specification Based on Seasat A Satellite Scatterometer and Conventional Winds for Driving an Ocean Wave Model

R. LALBEHARRY, M. L. KHANDEKAR, AND S. PETEHERYCH

Meteorological Services Research Branch, Atmospheric Research Directorate
Atmospheric Environment Service, Downsview, Ontario, Canada

This study examines the utility of remotely sensed Seasat A satellite scatterometer (SASS) winds for driving a spectral ocean wave model. The SASS winds are integrated with the conventional ship winds using an objective analysis scheme which employs the method of successive correction, modified to account for the variable data density, data quality, and the application of an elliptical weighting function. The analyzed winds are produced initially on a Cartesian grid over the North Atlantic and are then transformed onto a spherical orthogonal grid for input to a spectral ocean wave model. The model products are examined and validated against the observed ship and remotely sensed wave data to assess the impact of SASS winds on ocean wave analysis and modeling. Our study demonstrates that the integration of SASS winds into the wind analyses can provide improved wind inputs for validating wave models in a hindcast mode. The model wave heights when validated against the comparison data show a reduction in the root mean square error of up to 25% with the assimilation of SASS winds in the wind analyses. The ultimate goal of this study is to develop suitable algorithms for incorporating satellite-sensed wind and wave data into operational ocean wave models.

1. INTRODUCTION

The short-lived satellite Seasat (June 28 to October 10, 1978) provided valuable wind and wave data for approximately 100 days over the North Atlantic Ocean. On board the satellite, an oblique-viewing microwave radar known as the Seasat A satellite scatterometer (SASS), was used to sense high-resolution over-water winds in approximately 1400-km swaths extending across the subsatellite tracks.

The scatterometer radar measures backscattered energy from capillary-gravity waves of wavelengths of the order of 1–6 cm. The Seasat scatterometer was able to produce a unique solution for the neutral wind speed. The number of possible wind directions on which the vector wind solution is based varied from 2 to 4. A technical description of the satellite and its functioning may be found in the work by *Jones et al.* [1982], while the characterization of the algorithm relating the wind vectors to the normalized radar cross section used to derive the SASS winds can be found in the work by *Schroeder et al.* [1982]. A description about how the alias can be removed is given by *Wurtele et al.* [1982].

In recent years, several studies have investigated the utility of SASS winds, particularly for numerical weather prediction. *Aune and Warner* [1983], *Baker et al.* [1984], *Duffy et al.* [1984], and *Yu and McPherson* [1984] overall found rather small improvement to model results based on the impact of Seasat wind data. The impact was, however, found to be larger in southern hemisphere analysis than in northern hemisphere analysis. *Anthes et al.* [1983], in a series of model simulations to predict the Queen Elizabeth II (hereafter called QE2) storm, found significant improvement when supplementary SASS wind data were added to the initial conditions. *Duffy and Atlas* [1986] allowed the subjectively dealiased SASS winds to influence the upper levels of the atmosphere by means of a vertical correlation function and found a major forecast improvement of the QE2 storm. *Cardone* [1983] subjectively assimilated the SASS winds into a high-resolution spectral ocean wave model and obtained sea states closer to the observed sea states near the location of the oceanliner QE2 during and after explosive development of the QE2 storm.

The scatterometer data also make a positive impact on the analysis and forecast of meteorological systems. *Offiler* [1982] demonstrated the usefulness of SASS winds in the accurate placing of a marine frontal system. *Peteherych et al.* [1988] studies the impact of adding scatterometer winds to short-range analysis and forecast and found that meteorological features such as high- and low-pressure centers, ridges, troughs, shear zones, and cols were more clearly and accurately defined with the inclusion of these winds. The SASS winds therefore aid in the accurate description and placement of surface meteorological systems and provide an opportunity for improving both numerical weather and wave predictions by furnishing more complete initial conditions.

The purpose of this study is to objectively integrate the SASS winds with the conventional ship winds in order to develop an appropriate wind field for driving a spectral ocean wave model. The objective analysis procedure used for integrating the SASS winds with the conventional ship winds is described in section 3. The assimilated wind field is used to drive a spectral ocean wave model developed by *Resio* [1981] and hereafter referred to as the Resio wave model. The model outputs are evaluated against the marine surface observations as well as against the remotely sensed measurements, and the results of this evaluation are presented and discussed in section 4. Based on this evaluation, the impact of the SASS winds on ocean wave analysis and modeling is assessed, and the utility of the satellite-sensed winds for operational wave analysis and modeling is considered.

2. WIND AND WAVE DATA

The data sets used in this study are for the period September 8–19, 1978, for the North Atlantic bounded by

Paper number 89JC01641.
0148-0227/90/89JC-01641$05.00

TABLE 1. Description of the Four Different Gridded Wind Specifications for Input to the Ocean Wave Model and Definition of Symbols Used for the Corresponding Model-Generated Significant Wave Heights (SWH)

Model Input	Description	Model Output	Symbol
SASS wind	Corrected first-guess wind field using dealiased SASS winds only	SASS SWH	H_S
Ship wind	Corrected first-guess wind field using the irregularly spaced ship winds only	ship SWH	H_c
Mixed wind	Corrected first-guess wind field using the dealiased SASS and the irregularly spaced ship winds as a merged data set	mixed SWH	H_M
Blended wind	Wind field obtained by weighting the grid point values of SASS winds with those of ship winds	blended SWH	H_B

latitudes 30°N and 70°N and longitudes 20°W and 70°W. These are as follows.

1. Subjectively dealiased SASS winds described by *Peteherych et al.* [1984] and *Wurtele et al.* [1982] and available only for 15 days for the period September 6–20, 1978.

2. Marine surface wind and wave data from ocean weather ships, ships of opportunity, and buoys taken at the main synoptic hours.

3. A subset of the hindcast surface geostrophic winds from the Geostrophic Wind Climatology data set of the Atmospheric Environment Service of Canada, calculated from the Fleet Numerical Oceanography Centre gridded postsurface pressure analyses at 6-hour intervals and described by *Swail* [1985].

4. Significant wave height (SWH) charts produced operationally by the Meteorology and Oceanography (METOC) Centre, Halifax, Nova Scotia, for the northwest Atlantic; also SWH data from Seasat A altimeter sensor available for the period September 16–19, 1978. These two data sets serve as comparison data sets for evaluation of the model-generated wave heights. The other model parameters, namely, wave period and the wave/swell directions, are not validated in this study because (1) the reported values of these parameters are too sparse and (2) an examination of the reported wave periods indicate that these values are not too reliable for inclusion in a quantitative error analysis. Consequently, the validation is made against the most commonly used and readily available parameter, the SWH.

In operational meteorological analysis, a time window of ±3.0 hours is generally used, and all data within this time window are considered to be synoptic. Satellite data, however, are asynoptic in nature. The SASS winds with resolution of the order of 100 km and a mean wind speed of 10 m/s would be equivalent to an averaging time of about 2.8 hours and hence provides a more accurate representation of the synoptic scale winds than the ship and buoy winds. The interpolated grid point value is a weighted average of all observations lying within an assigned radius of influence about the analyzed grid point. This results in further spatial smoothing of the observations, so that application of time weights to the observations within ±3.0 hours from analysis time does not seem necessary. For this reason, and to simulate operational conditions, the SASS winds within ±3.0 hours from analysis time are treated in this study as synoptic. For a satellite pass lying between 3.0 and 5.0 hours and between −3.0 and −5.0 hours from analysis time, the observations are incorporated into the analysis but with a reduced influence through the application of time weights. For SASS times up to ±3.0 hours a weight of 1.0 is applied, and this is reduced to 0.8 and to 0.6 for SASS times of ±4.0 and ±5.0 hours from analysis time, respectively. In the domain of interest, nearly all the Seasat tracks lie within ±3.0 hours from the analysis times.

The first-guess wind field for use in the interpolation technique is estimated from the surface geostrophic winds through use of a reduction-rotation model. As suggested by *Low and Swail* [1985] for open-water wind approximation, the geostrophic wind speed is reduced by 15% and its direction rotated counterclockwise by 20°, which is a simple empirical procedure to consider the influence of boundary layer processes on the wind flow and is generally applicable to a boundary layer representing neutral to unstable conditions. This reduction-rotation of the geostrophic wind provides a first approximation of the surface wind. The surface wind field so derived is now used as the first-guess surface wind field, which is then modified by the observations to obtain a corrected surface wind field to drive an ocean wave model.

The wind field at grid points, called the gridded wind field, is derived through the application of the method involving successive modifications to the first-guess wind field. Modifications using only the dealiased SASS winds generate the gridded SASS winds, those using only the irregularly spaced conventional ship winds give the gridded ship winds, and those using a merged data set of both the dealiased SASS and irregularly spaced ship winds produce the gridded mixed winds. Further, the gridded SASS winds are blended with the gridded ship winds using an appropriate weighting scheme (described in section 3) to generate the gridded blended winds. Table 1 describes the various wind inputs to the wave model and defines the symbols used for the corresponding model-generated SWH.

The METOC SWH analysis procedure makes use of the ship reports of wind and sea states, the previous 6-hour SWH analysis, the 12-hour sea state forecast valid for that analysis time, and the surface pressure analysis to produce the SWH chart at analysis time for the northwest Atlantic [see *Morgan*, 1971]. A high level of quality control is used in the preparation of the METOC charts. In a recent study by *Pickett et al.* [1986], eight operational wave model analyses were compared with the GEOSAT satellite wave height observations over the northwest Atlantic for selected days. Among the wave models considered in Pickett's study were the wave models of the Federal Republic of Germany, the Netherlands, U.S. Navy, NOAA, and the wave height charts produced by the METOC. The study indicates that the root-mean-square error (rmse) of the METOC wave heights is about 1.5 m and that this rmse value is found to be comparable with the corresponding rmse values generated

by some of the other operational wave models. A similar wave model intercomparison study by *Khandekar et al.* [1986] demonstrates that the METOC wave height charts provide the closest agreement with the buoy-measured wave heights in the Canadian Atlantic with a correlation coefficient of 0.83 between the two. The METOC charts, in our opinion, represent the best available areal coverage of wave height information over the northwest Atlantic and have therefore been chosen as one of the comparison data sets to evaluate the model results. It may be noted that for the Seasat period no other synoptic scale wave height data over the northwest Atlantic were available.

The operationally produced METOC chart covers the domain bounded roughly by latitudes 35°N and 65°N and longitudes 25°W and 70°W. The Resio model grid is superimposed on the analyzed 0000 and 1200 UT wave charts, and the SWHs are subjectively interpolated at the model grid points in the analysis domain. These grid point values are then merged with the ship-observed wave heights, and the combined data set is then used to objectively obtain values at those model grid points lying outside the METOC analysis area. A simple linear interpolation scheme is used to generate the 0600 and 1800 UT wave height fields from the gridded 0000 and 1200 UT height fields. These wave fields, denoted by H_0 and identified as METOC SWH, serve as one of two comparison data sets used in this study, while the Seasat altimeter wave data as described below serve as the other set.

The Seasat altimeter is a nadir-viewing, short-pulse, 3-ns active microwave radar operating at 13.5 GHz and emitting electromagnetic pulses at the rate of 1000 s^{-1}. Backscattered energy from specular reflection by the surface immediately below the satellite is transmitted to the altimeter. The diameter of the area of interaction between the pulse and the sea surface is about 2.4 km in a calm sea and increases to about 12 km in high seas. The effective interaction area increases as the wave height increases, and this has the effect of stretching out the return pulse front. The return signal is then fitted to a model curve, which varies with wave height. To reduce curve-fitting errors, a mean curve is obtained by averaging the return signals from as many as 1000 pulses, and the SWH is deduced from the mean shape of this curve. The Seasat radar altimeter SWH, denoted by H_A, is given every second along the subsatellite tracks. The H_A values are arranged in sets of four consecutive values. The mean SWH value of each set is found and assigned to a mean latitude/longitude along-track location. The ground speed of Seasat is 6.6 km/s, so that the averaged altimeter values are given at intervals of about 26 km along the track. The two outputs of the model hindcast wave heights closest to the time of the orbit chosen are linearly interpolated to obtain the model SWHs corresponding to the mean track time over the grid area. A grid box along the track may contain several altimeter values. The model SWH values at the four corners of the box are then distance weighted to obtain the interpolated value at each of the H_A locations within the box. A comparison of the Seasat altimeter wave data with the buoy-measured waves [*Jet Propulsion Laboratory*, 1980] and with wave observations from ships over the North Atlantic [*Queffeulou*, 1983] reveals a standard deviation $\leq$1 m in both cases.

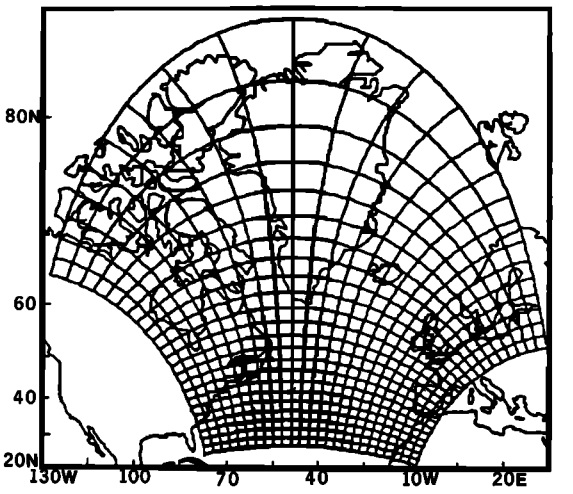

Fig. 1. The specially designed spherical orthogonal grid (SOG) for the Resio spectral ocean wave model with grid spacing of 277.7 km in each direction. East-west grid lines follow great circle paths, and the intersections of the grid lines are orthogonal.

3. Data Analysis Techniques

3.1. *Interpolation Method*

The Resio wave model used in this study is a second-generation spectral ocean wave model in which the nonlinear wave-wave interaction term is used in a parameterized form. *Resio* [1981] develops a functional relationship between the Phillips equilibrium constant and a nondimensional fetch and obtains an expression for the nonlinear source term which involves the square of the wind speed. Further, Resio neglects the linear growth term, so that the net source term consists of the exponential growth term and the parameterized nonlinear wave-wave interaction term. The model assumes that waves are already present initially, so that the wave-wave interaction term becomes operative and generates more waves. A local nonpropagating parametric model with a moderately high-frequency cutoff is incorporated so as to remove excess waves. The boundary between the parametric and the discrete spectral domains of the model is maintained at a fixed point, and energy in each domain is conserved independently. More details of the model can be found in the work by *Resio* [1981]. In subsequent studies, *Resio* [1982] has demonstrated the utility and reliability of his model for application in the Canadian Atlantic, while *Penicka* [1986] has amply demonstrated the sensitivity of the Resio model to wind specification. The Resio model is chosen because of its simplicity, minimal computational requirements, its sensitivity to wind specification, and its ability to produce reliable results when driven by accurate wind fields.

Figure 1 shows the 26 × 24 specially designed spherical orthogonal grid (SOG) used by the Resio model with a grid spacing of 277.7 km (=2.5° latitude) in each direction. In this grid the axes are curvilinear, allowing east-west grid lines to follow great circle paths and each intersection of grid lines to be orthogonal. The irregularly spaced wind data are initially interpolated onto a 24 × 23 Cartesian grid using the successive correction method (SCM) of *Cressman* [1959]. This grid is a polar stereographic projection (true at 60°N) with grid spacing of 277.7 km in each direction and is shown in Figure

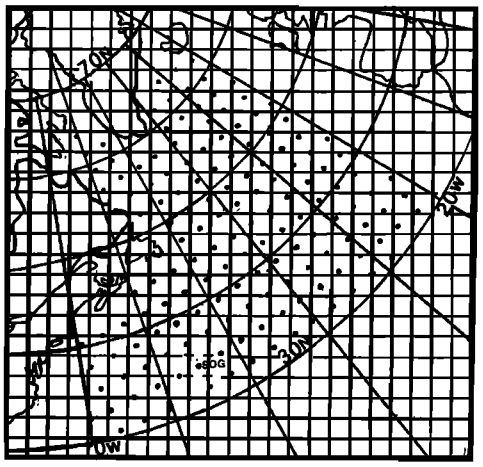

Fig. 2. Cartesian grid onto which the wind data are initially interpolated with grid spacing of 277.7 km in each direction. The dots are the subset of the SOG points in Figure 1 onto which the wind data on the Cartesian grid are transformed for input to the wave model.

2 with a subset of the SOG points (dots) which lie in the area of the North Atlantic Ocean bounded by latitudes 30°N and 70°N and by longitudes 20°W and 70°W and at which wind specification is required for input to the Resio wave model. The wind fields described in section 2 are all initially specified on the Cartesian grid, and the gridded data are then transformed onto the SOG grid by bilinear interpolation of the four Cartesian grid points surrounding each SOG point.

The essential steps of *Cressman*'s [1959] SCM are described by *Seaman* [1983]. In our study the SCM is modified to incorporate the application of quality control of observations with gross errors, the effect of data density, and the application of an elliptical weighting function to allow for upwind/downwind observations to have greater weight than crosswind observations. The first guess field is successively corrected three times using the formulation

$$\Delta G_k = \sum_{i=1}^{N} b_{ik} f_{ik} \Big/ \sum_{i=1}^{N} b_{ik} \tag{1}$$

where k is the scan number and is equal to 1, 2, and 3, respectively. For the kth scan, N is the total number of observations influencing the analyzed grid point, b_{ik}, the weight given to the ith observation, f_{ik}, the deviation of the observation from the interpolated guess field at the ith point, and ΔG_k, the correction to be added to the first-guess field.

A quality control procedure is applied that uses as rejection criterion a comparison of a given difference with the standard deviation s_k of the N differences influencing the analyzed grid point. If $|f_{ik}|$ is less than $2s_k$, the observation is used in the assimilation without modification. If $|f_{ik}|$ lies between $2s_k$ and $3s_k$, f_{ik} is modified to a value equal to $\bar{f} \pm 2s_{ik}$, where $\bar{f}$ is the mean of the N differences. For $|f_{ik}|$ greater than $3s_k$, the difference is not entirely neglected, but it is arbitrarily adjusted to a value equal to $0.12f_{ik}$. In this way, useful data are not discarded, and the rejection criterion utilizes to some extent the error structure of the deviations influencing the analyzed grid point. For a normal distribution, less than 5% of the deviations are modified, and these are likely to result from observations with gross errors.

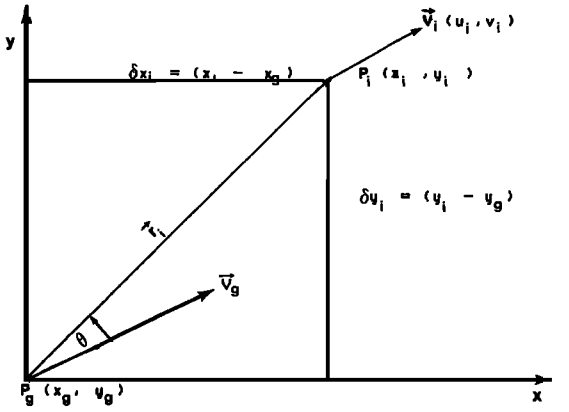

Fig. 3. Configuration of the variables used in the elliptical weighting function in the Cartesian grid coordinate system. P_g is the grid point, and P_i the observation point.

The elliptical weighting function for the kth iteration was developed by *Benjamin and Seaman* [1983] and is of the form

$$b_i = [(R^2 - d_i'^2)/(R^2 + d_i'^2)] \qquad d_i' < R$$
$$b_i = 0 \qquad d_i' \geq R \tag{2}$$

where

$$d_i'^2 = \delta x_i'^2/E^2 + \delta y_i'^2$$
$$\delta x_i' = (\delta x_i u_i + \delta y_i v_i)/V_i \tag{3}$$
$$\delta y_i' = (-\delta x_i v_i + \delta y_i u_i)/V_i$$

The elongation factor E is the *Inman* [1970] function defined by

$$E^2 = 1 + \beta \cos^2 \theta \tag{4}$$

where β is a nondimensional ratio of the wind speed relative to a maximum wind speed as given by

$$\beta = V_g/V_{\max} \tag{5}$$

The geometric relationship of these variables is portrayed in Figure 3. Here u_i and v_i are the x and y components of the observed velocity vector, respectively, at the ith observation point in the Cartesian grid, V_g is the grid point wind speed, $V_{\max}$ is the observed maximum wind speed in the analysis area at analysis time, and θ is the angle between the position vector $\mathbf{r}$ and the flow velocity vector $\mathbf{V}_g$, at the grid point. The application of the elliptical weighting function is illustrated in Figure 4. Observation points 1–4 are equidistant from the analyzed grid point P_g, at which the flow direction is given by the wind vector $\mathbf{V}_g$. The points all lie within the influence radius R, with 1 and 3 located downwind and upwind, respectively, and 2 and 4 crosswind from P_g. E^2 is set equal to 1 for any combination of β and θ giving $E^2 < 1.375$, and the weighting function, b in (2), degenerates into a circular one, resulting in the same weight being applied to all observations satisfying this condition and equidistant from the analyzed grid point. For $E^2 \geq 1.375$, d is modified and the isopleths of b generate ellipses with the major axes along the flow direction. The crosswind stations 2 and 4 in

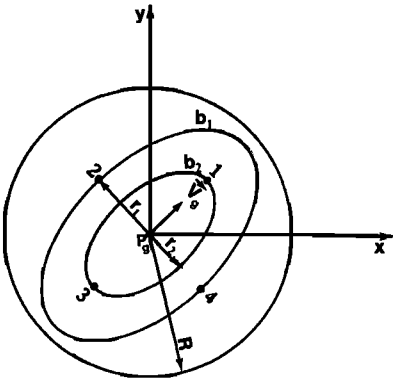

Fig. 4. Schematic diagram of the weight isopleths for the elliptical weighting function for the flow direction given by the wind vector $\mathbf{V}_g$ at the grid point P_g. See text for details.

this case receive weights of b_1 corresponding to a circular weighting function having a radius r_1, while the downwind/upwind points 1 and 3 receive weights b_2 corresponding to a circular weighting function having a radius r_2, with $b_2 > b_1$. Any station at a distance r_1 from P_g is given a weight b such that $b_1 \leq b \leq b_2$ with the constraint that the combination of β and θ gives $E^2 \geq 1.375$; otherwise, $b = b_1$. For instance when $\beta = 1$, θ must lie within 0° ± 52° or 180° ± 52°, and when $\theta = 0°$ or 180°, β must be ≥0.375. This procedure allows upwind/downwind observations to have greater weights than crosswind observations in regions of relatively strong wind, defined here as the wind whose speed is at least 0.375 times the observed wind speed maximum at analysis time in the analyzed area.

The radius of influence R_k for the kth scan is expressed as a function of data density in the form

$$R_k = c_k\, d \tag{6}$$

where c_k = 1.6, 1.4, and 1.2 for scan k = 1, 2, and 3, respectively [see *Stephens and Stitts*, 1970], and

$$d = (\pi/M)^{1/2} r_d \tag{7}$$

is the average distance between the data points computed for the M observations found in a circle of radius r_d centered at each grid point. Here, r_d is chosen as 833 km (= 3 grid units), since the spatial correlation coefficient is still greater than zero, being about 0.3 for SASS winds and about 0.1 for ship winds at this separation distance [*Brown and Swail*, 1988]. The number of data points affecting a particular grid point is determined on the basis of data density. Although R_k is modified for data density, it is not allowed to become less than 277 km, so that all data within this radius enter the analysis. If M is less than 12, all data within r_d are used. If M is greater than or equal to 12 but the number of observations within R_k is less than 12, R_k is increased until N is greater than or equal to 12. This minimum number corresponds closely to the station distribution about a grid point generally used by other investigators in numerical experiments employing optimum interpolation techniques. Since the observations within r_d are sorted in order of distances from the analyzed grid point, N gives for the kth scan the number of observations nearest to the grid point.

3.2. *Interpolation Error Analysis*

Let the superscripts, A, i, o, P, denote the analyzed, interpolated, observed, and first-guess values, respectively, and the subscripts i and g the observed point and the grid point, respectively. Given the observed field F_i^o at irregularly spaced points, the first-guess field F_g^P at grid points, and the interpolated first-guess field F_g^{iP} at observation points, the analyzed grid point value is obtained by making corrections based on available data to the first-guess value using the standard interpolation equation

$$F_g^A = F_g^P + \sum_{i=1}^{n} w_i (F_i^o - F_g^{iP}) \rightarrow f_g^A = \sum w_i (f_i + \varepsilon_i) \tag{8}$$

where f_g^A is the analyzed grid point correction expressed as the difference between the analyzed and first-guess values, f_i is the true increment between the observed value and the interpolated guess field at the ith observation point, ε_i is the observational error, w_i is a noniterative weight, and n is the number of observations influencing the grid point. If f_g is the true grid point correction, then the mean square interpolation error [*Seaman*, 1983; *Bergman and Bonner*, 1976] is given by

$$[E_g^2] = [f_g^2] - 2 \sum_{i=1}^{n} w_i [f_g f_i] + \sum_{i=1}^{n} \sum_{j=1}^{n} w_i w_j [f_i f_j] + \sum_{i=1}^{n} w_i^2 [\varepsilon_i^2] \tag{9}$$

where the square brackets denote an average over many realizations. The assumption is made that the random observational errors are unrelated to each other, that is, $[\varepsilon_i \varepsilon_j] = 0$ for $i \neq j$ and $= [\varepsilon_i^2]$ for $i = j$, and unrelated to the true values of the measured quantities, that is, $[f_g \varepsilon_i] = [f_i \varepsilon_j] = [f_j \varepsilon_i] = 0$. For unbiased errors, $s^2 = [f_g^2]$ is the error variance of the initial guess value from the true value at the grid point, and for homogeneous variance, $s^2 = s_{f_i}^2 = s_{f_j}^2$. With these assumptions, (9) reduces to

$$[E_g^2]/s^2 = 1 - 2 \sum w_i \mu_{gi} + \sum \sum w_i w_j \mu_{ij} + \sum w_i^2 \lambda^2 \tag{10}$$

Equation (10) provides a measure of the interpolation error. The parameter $\lambda^2 = [\varepsilon_i^2]/s^2$ is the normalized observational error variance, μ_{gi} is the spatial correlation coefficient between the deviation at the grid point and the deviation at the ith observation point, and μ_{ij} is the spatial correlation coefficient between the ith and jth observational deviations within the radius of influence of the analyzed grid point. The spatial correlation coefficients are assumed to be homogeneous and isotropic in character and hence can be expressed as a function of separation distance only. It is more convenient to model the spatial correlation function by a mathematical expression. A spatial correlation study of SASS and ship winds over the northwest Atlantic by *Brown and Swail* [1988] for the period September 6–20, 1978, suggests that the correlation function can be approximated by the Gaussian function given by

$$\mu = \exp(-q^2/2L^2) \tag{11}$$

where q is the separation distance between pairs of observations and/or between a grid point and an observation point

and L defines a length scale for which $\mu = 1/e$. The study also indicates that $L \simeq 650$ km for SASS winds, $\simeq$500 km for ship winds, and $\simeq$580 km for the combined SASS and ship winds.

The noniterative weights w_i are computed for each grid point using the SCM. For a given scan the observations influencing the analyzed grid point are determined, and the contribution by the ith observation to the grid point correction is found. The process is repeated for each scan using the same observed value but with the updated first-guess field. The algebraic sum of the corrections for all scans gives the total contribution of the ith observation to the grid point correction, and this allows the resultant weight of the ith observation to be determined. The noniterative weights are computed for all the observations influencing the grid point and are then normalized. The fractional interpolation error in (10) is then estimated using the normalized weights, the modeled spatial correlation function, and specified values of the fractional observational error.

3.3. *Field Blending*

Given adequate spatial and temporal distributions of SASS and conventional ship winds, a method to blend the analyzed grid point values of SASS winds X_g^A with those of the ship winds Y_g^A is described. An estimate of the blended value at the grid point location can be given by

$$Z_g^A = aX_g^A + bY_g^A \tag{12}$$

where a and b are appropriate weights. For unbiased estimates $[Z_g] = [Z_g^A] = [X_g^A] = [Y_g^A]$ and from (12) this gives $a + b = 1$. Z_g is the true grid point value, and $[Z_g]$ can be considered as the norm. Removal of the norm reduces (12) to

$$z_g^A = ax_g^A + by_g^A \tag{13}$$

where the lower case letters x, y, and z refer to deviations from the norm. If z_g is the true deviation of the blended value, then the mean square error is given by

$$[E_z^2] = s^2 - 2s(as_1R_1 + bs_2R_2) + a^2s_1^2 + b^2s_2^2 + 2abs_1s_2r \tag{14}$$

Here, R_1 is the correlation coefficient between z_g and x_g^A, R_2 that between z_g and y_g^A, and r that between x_g^A and y_g^A. Also, s^2 is the variance of the blended field, s_1^2 that of the SASS wind field, and s_2^2 that of the ship wind field. Under the assumption of homogeneous variance, $s^2 = s_1^2 = s_2^2$. Minimization of the mean square error gives a and b in terms of R_1, R_2, and r, and for $R_1 \simeq R_2$, (14) reduces to

$$[E_z^2]/s^2 = 1 - 2R_1R_2/(1 + r) \tag{15}$$

For only SASS winds, $a = 1$ and $b = 0$ and (14) reduces to

$$[E_x^2]/s^2 = 2(1 - R_1) \tag{16}$$

Similarly, for only ship winds, $a = 0$ and $b = 1$, and (14) becomes

$$[E_y^2]/s^2 = 2(1 - R_2) \tag{17}$$

The weighting factors a and b, derived by minimizing the mean square error in (14), are then normalized to give

$$a' = (R_1 - R_2r)/[(R_1 + R_2)(1 - r)]$$
$$b' = (R_2 - R_1r)/[(R_1 + R_2)(1 - r)] \tag{18}$$

If the initial guess field is considered as the norm, then an approximation to (13) can be obtained from the merged data set expressed as

$$z_g^A = \sum_{i=1}^{n} w_i(x_i + \varepsilon_i) + \sum_{k=1}^{m} c_k(y_k + \varepsilon_k) = \sum_{i=1}^{n+m} p_i(x_i' + \varepsilon_i') \tag{19}$$

where n and m are the numbers of dealiased SASS and irregularly spaced ship winds influencing the analyzed grid point, respectively, and all deviations are with respect to the norm. Equation (19) is of the same form as (8), in which x' replaces f and is either SASS wind deviation x or ship wind deviation y, and p and ε' are the corresponding weight and observational error, respectively. Using (10) separately for the merged, SASS, and ship winds, estimates of $[E_z^2]/s^2$, $[E_x^2]/s^2$, and $[E_y^2]/s^2$ are obtained. Substitution of these values in (15)–(17) gives R_1, R_2, and r, and using (18), a' and b' are estimated. The assumption is made that the fractional interpolation error due to the blended field is the same as that due to the merged field in order to estimate r from (15). The objectively derived weighting factors are then used to blend the grid point values of SASS winds and ship winds.

4. Results and Evaluation

We present in this section some of the important results for two hindcast periods, namely, September 9–13, and 16–19, 1978, respectively. Additional results of this study can be found in the work by *Lalbeharry* [1988].

The fractional error variance $[E^2]/s^2$ is the ratio of the interpolation error variance to the total error variance of the initial guess field from the true field. It is computed for each of the 552 grid points of the Cartesian grid for the normalized variances of observational error of $\lambda^2 = 0$, 0.1, and 0.25. A value of $\lambda^2 = 0$ implies perfect observations, while $\lambda^2 = 0.1$ implies that the observational error variance accounts for 10% of the error variance of the initial guess field from the true field and its effect is to inflate the interpolation error variance $[E^2]$ at the analyzed point. The areal mean is then computed using those points for which $[E^2]/s^2 < 0.90$. The majority of points have values far below 0.90. Grid points with values $\geq$0.90 are indicative of points being influenced by very few observations, generally far away from the analyzed grid point. These points and those not influenced by any observations are excluded from the computation of the areal mean of the fractional error variance. The results for $\lambda^2 = 0.1$ are tabulated in Table 2 and are used in the computations of the weighting factors.

In Table 2 the value $[E^2]/s^2 = 0.215$ for SASS winds at 1200 UT on September 10 indicates that the areal mean interpolation error variance is near 22% of the total error variance of the initial guess field from the true field. The overall areal mean of $[E^2]/s^2$ is 0.25 for SASS winds, 0.37 for ship winds, and 0.20 for mixed winds. Using (15)–(17), these results give the corresponding correlation coefficients $R_1 = 0.88$, $R_2 = 0.81$, and $r = 0.76$, respectively. Substitution of these values in (18) gives the weight $a' = 0.64$ for SASS winds and the weight $b' = 0.36$ for ship winds.

The fractional interpolation error has a functional depen-

TABLE 2. Areal Average of Fractional Interpolation Error Variance for SASS Winds, Ship Winds, and Mixed Winds Corresponding to the Fractional Observational Error Variance $\lambda^2 = 0.1$ and Length Scale $L = 650$ km for SASS Winds, 500 km for Ship Winds, and 580 km for Mixed Winds

	Analysis Period 1 September 8–13, 1978				Analysis Period 2 September 15–19, 1978			
Day	Hour, UT	SASS	Ship	Mixed	Day	Hour, UT	SASS	Ship	Mixed
Sept. 8	1200	0.259	0.361	0.190	Sept. 15	0000	0.258	0.375	0.203
Sept. 9	0000	0.295	0.401	0.260		1200	0.294	0.336	0.195
	1200	0.269	0.374	0.199	Sept. 16	0000	0.245	0.391	0.211
Sept. 10	0000	0.179	0.415	0.205		1200	0.256	0.353	0.192
	1200	0.215	0.364	0.187	Sept. 17	0000	0.217	0.396	0.187
Sept. 11	0000	0.233	0.407	0.205		1200	0.257	0.345	0.180
	1200	0.254	0.357	0.184	Sept. 18	0000	0.237	0.376	0.201
Sept. 12	0000	0.240	0.367	0.205		1200	0.301	0.330	0.212
	1200	0.293	0.352	0.213	Sept. 19	0000	0.253	0.346	0.198
Sept. 13	0000	0.230	0.388	0.193		1200	0.266	0.360	0.191
Average		0.247	0.379	0.204			0.258	0.361	0.191

dence on the weights, the spatial correlation coefficient, and the observational error. The weights are modified for data density, while the correlation coefficient depends also on the length scale L, which as mentioned earlier, is 650 km for SASS winds, 500 km for ship winds, and 580 km for mixed winds. Interpolation errors therefore tend to be lower for the more closely spaced observations of SASS winds and mixed winds because of the higher spatial correlation coefficient and resolution of the SASS winds as opposed to the ship winds. The error analysis of Table 2 seems to suggest that SASS winds and mixed winds can provide a more accurate description of the wind field than that provided by the conventional ship winds.

4.1. *Hindcast Period September 9–13, 1978*

During the period September 9–13, 1978, altimeter wave data were not available, so that evaluation of the model wave hindcasts are made against METOC SWH analyses described in section 2. The main wave generation event in this period was the QE2 storm which deepened explosively from a central pressure of 1008 mbar at 1200 UT on September 9 to 950 mbar at 1200 UT on September 10 with peak winds of 30 m/s in the south quadrants. However, by 1200 UT on September 11 the central pressure rose to 976 mbar, and peak winds dropped to about 27.5 m/s as SWH continued to build and the area of high winds about the storm expanded. Figure 5 [from *Cardone*, 1983] gives the relative tracks of the QE2 storm and the oceanliner QE2. The ship took evasive action after it encountered about 11-m-high waves around 1200 UT on September 11. Figure 6 (also from *Cardone* [1983]) is a subjective analysis of the observed SWH valid at 0600 UT on September 11 and shows that the ship was already in an area of high seas and was being battered with waves greater than 6 m high.

Figure 7 shows the spatial distribution of the subjectively dealiased SASS winds and the observed storm center location denoted by the letter "X." The storm center is evident in the SASS winds, especially for pass 1080. Relatively large data-void areas exist between successive passes, and in order to adequately specify the wind field, some form of integration with the ship winds is required. If no SASS and ship winds influence a grid point, the first-guess wind remains unchanged. Since the first-guess wind fields are derived from postanalyses of the pressure fields, the uncorrected grid point values are still representative of the flow pattern. The objectively analyzed wind fields for four different wind inputs are illustrated for comparison in Figures

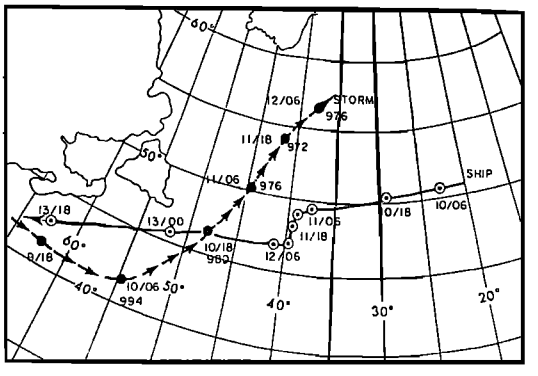

Fig. 5. Relative tracks of the QE2 storm and the luxury oceanliner QE2 [from *Cardone*, 1983]. The tracks show the positions of the ship and the storm center at the indicated day/hour (UT) and the central pressure of the storm in millibars.

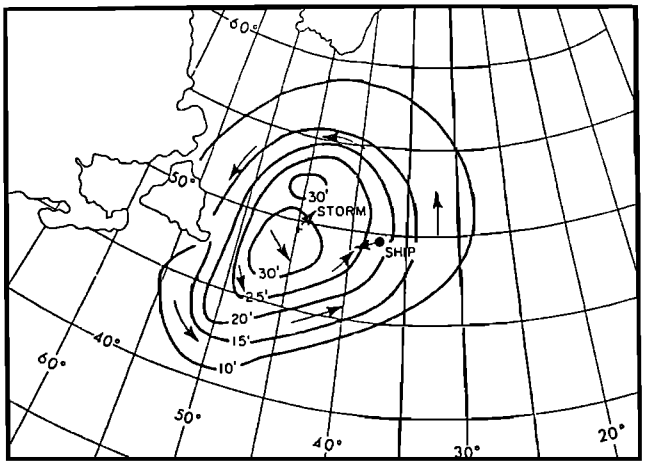

Fig. 6. Subjective analysis of the observed significant wave height in feet valid at 0600 UT September 11, 1978 [from *Cardone*, 1983].

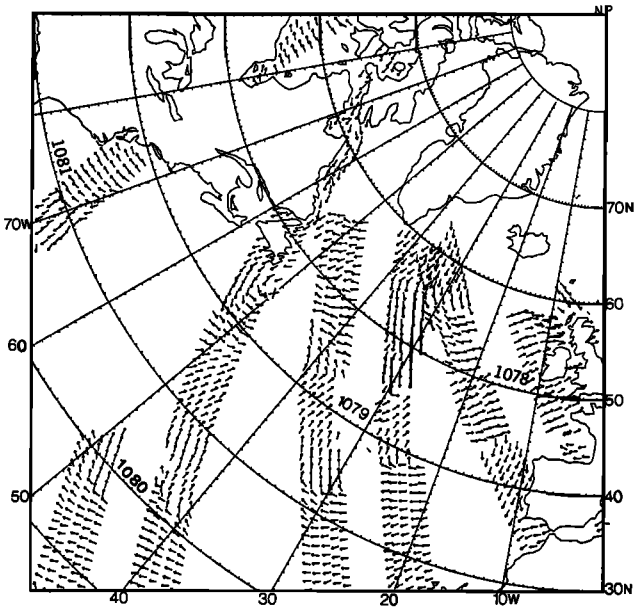

Fig. 7. Subjectively dealiased SASS wind vectors (not drawn to scale) over the North Atlantic centered at analysis time 1200 UT September 10, 1978, for orbits 1078–1081. The observed QE2 storm center location is denoted by the letter X.

8*a*–8*d* for 1200 UT on September 10 when the storm was at its mature stage.

Figure 8*a* indicates that the SASS winds give a more accurate description of the wind than that provided by the ship winds illustrated in Figure 8*b*, especially in areas influenced by the dealiased SASS winds shown in Figure 7. The major SASS wind speed peak ≈30 m/s occurs in the southwest quadrant of the storm during the mature stage. In contrast, the primary ship wind speed peak is ≈19 m/s, and the area enclosed by the 18 m/s isotach is much smaller than that given by the SASS winds. Both the mixed wind field in Figure 8*c* and the blended wind field in Figure 8*d* exhibit nearly the same structural features of the SASS wind field but with somewhat reduced speed amplitudes. The mixed wind field gives a peak speed of about 28 m/s, while the blended field gives about 26.5 m/s. In the mixed wind field the grid point value may be based only on dealiased SASS winds, while the blended value is a weighted average of the grid point values of the SASS and ship wind fields and this may account for the difference in peak amplitudes. The objectively derived wind field in Figure 8*c* is in closer agreement with *Cardone*'s [1983] base case wind field than with his operational surface wind field. His base case wind field was subjectively derived from combined SASS and conventional ship winds, while the operational surface wind field was derived from NMC final sea level pressure analysis. The peak mixed winds derived here and those in Cardone's base case wind field both occur in the southwest quadrant of the storm and lie in the range 28–30 m/s.

A sample of the comparison wave height data for September 11 valid at 0600 and 1800 UT is shown in Figures 9*a*–9*b*. These wave fields are derived from METOC charts as discussed in section 2 and have been identified as METOC SWH denoted by H_0. It is observed that the area of high H_0

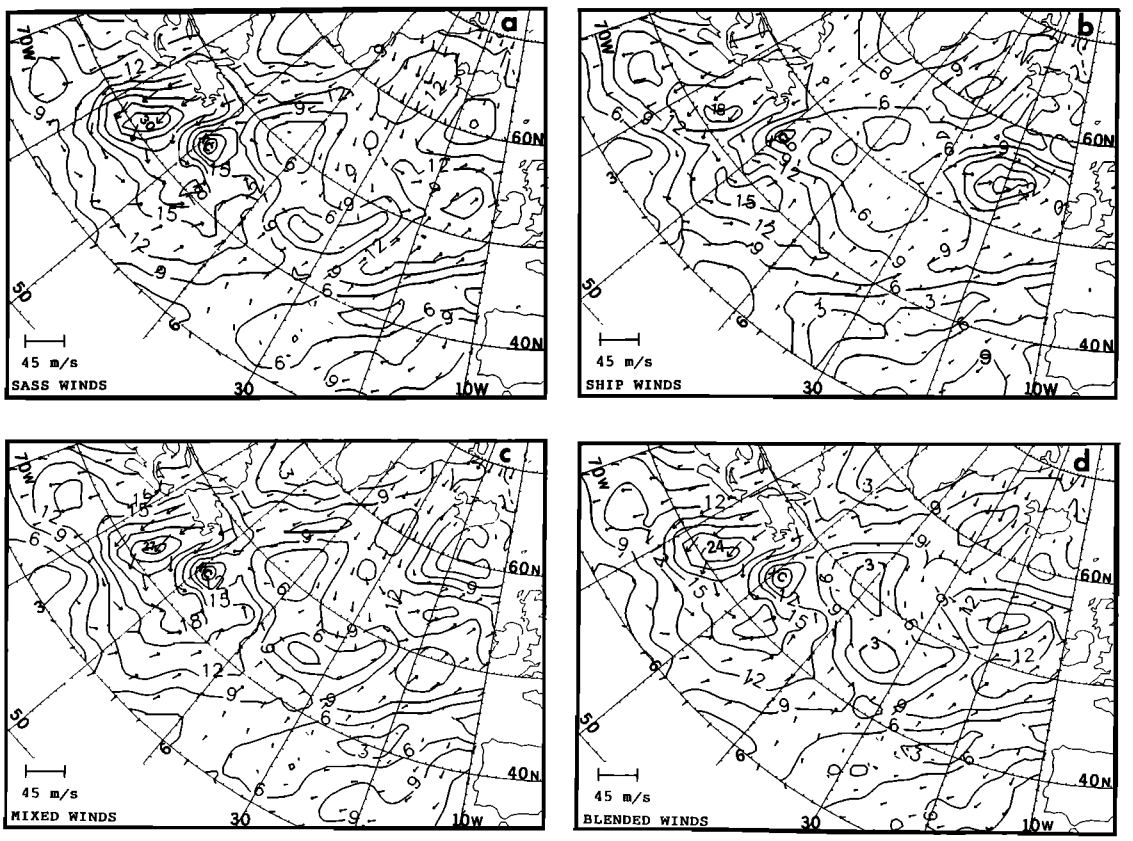

Fig. 8. The analyzed wind vectors valid at 1200 UT September 10, 1978, based on (*a*) only dealiased SASS winds, (*b*) only irregularly spaced ship winds, (*c*) mixed winds, and (*d*) blended winds. The vector length is proportional to the wind speed, and the arrows point toward the direction of flow. The solid lines are isotachs drawn at 3.0 m/s intervals. The analyzed QE2 storm center is denoted by the letter C and the observed center by X.

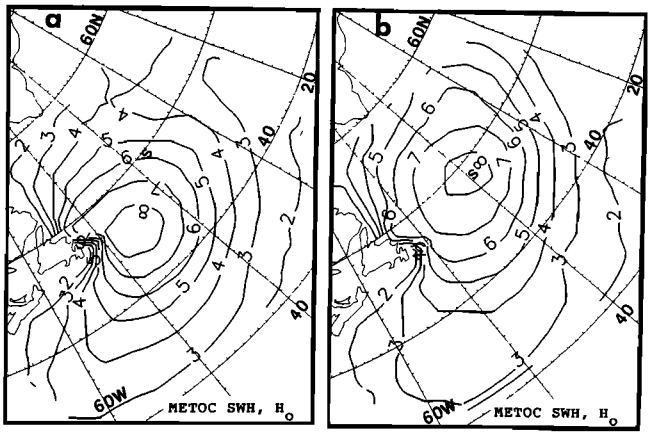

Fig. 9. Wave height contours (in meters) of the comparison data identified as METOC SWH and denoted by H_0 for September 11, 1978, at (*a*) 0600 UT and (*b*) 1800 UT. The locations of the oceanliner QE2 are denoted by the letter S.

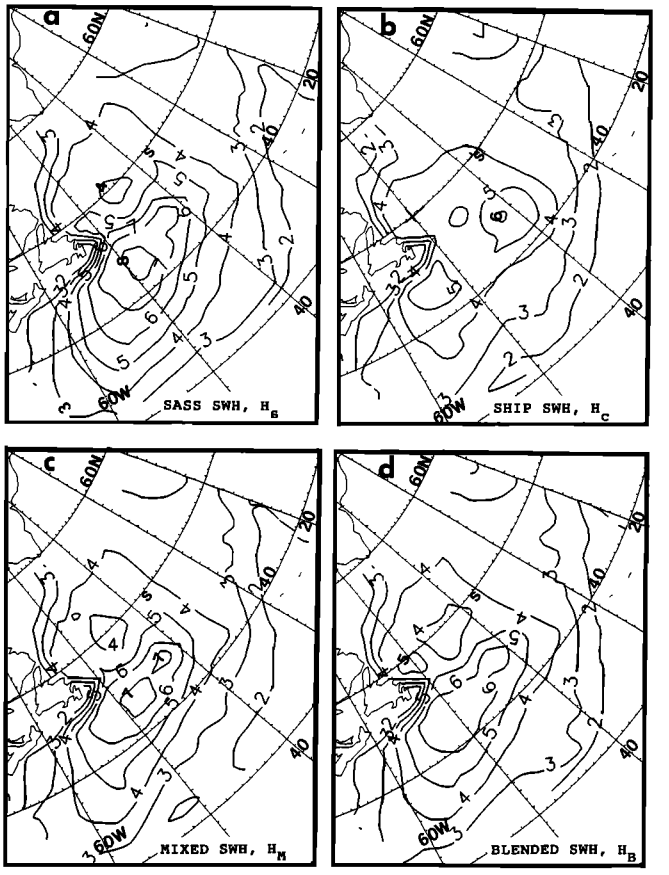

Fig. 10. Model hindcast wave height contours in meters for 0600 UT September 11, 1978, using as input (*a*) SASS winds, (*b*) ship winds, (*c*) mixed winds, and (*d*) blended winds. Model simulation starts at 1200 UT September 9, 1978. The initial wave state for each wind specification is provided by spinning up the model using the previous 24-hour mixed wind fields. The location of the oceanliner QE2 is denoted by the letter S.

moves toward the northeast. This movement is in the general direction of storm movement and lies south of the storm track shown in Figure 5, generally in the area of long fetch. Comparison of the METOC SWH in Figure 9*a* with subjective analysis of the wave height field in Figure 6 shows similarities in terms of wave height patterns and locations of areas of maximum SWH. Further, the oceanliner QE2, located near 49°N/39°W at 1200 UT on September 11, encountered wave heights which it visually estimated to be about 11 m. By 1800 UT on September 11 the ship was near 48°N/39.5°W, and at this time the METOC analysis in Figure 9*b* shows peak heights of about 9 m near the QE2, reflecting the high seas encountered by the QE2 6 hours earlier.

Each of the four wind specifications shown in Figures 8*a*–8*d* is used to drive the Resio wave model to simulate hindcast waves for an 84-hour period with wind input every 6 hours beginning at 1200 UT on September 9. The initial wave state for all wind inputs is provided at the start of each run by spinning up the model using the previous 24-hour mixed wind fields. A sample hindcast of the wave heights generated by each of the wind inputs is displayed in Figures 10*a*–10*d*. The wave height charts refer to 0600 UT September 11 after the model is driven a further 36 hours following the initial spin-up time of 24 hours.

A comparison of the 0600 UT model SWH analyses in Figures 10*a*–10*d* with the 0600 UT METOC analysis in Figure 9*a* shows that the model areas of high heights are not exactly coincident with the corresponding METOC area. However, the displacement error is larger for the ship SWH, H_c. The inclusion of SASS winds reduces the displacement error and makes the area of high heights more coincident and in closer agreement with the area based on the METOC analysis. Peak value of over 8 m is generated for SASS SWH, H_s, in Figure 10*a*, while that for H_c in Figure 10*b* is near 6 m. The peak value of mixed SWH, H_M, in Figure 10*c* is over 7 m. This amplitude is slightly lower than the peak H_s and reflects the effects of merging the two wind data sets. The results of the blended SWH, H_B, shown in Figure 10*d* are similar to the mixed SWH. Because of the weighting technique employed, H_B may show a slight reduction in the height amplitude as indicated in Figure 10*d*. The areas enclosed by the 6-m contour of H_s, H_M, and H_B are much larger than the corresponding area of H_c in Figure 10*b*. The wave heights H_c are underestimated when the conventional wind data do not adequately specify the storm intensity. The SASS winds therefore help to better define the storm intensity and hence provide a more accurate description of the model-generated wave heights.

A quantitative evaluation of the model-generated wave heights H is made against the comparison data identified as METOC SWH and denoted by H_0. The evaluation is done for 13 six-hourly map times from 1000 UT September 10 to 0000 UT September 13 after driving the model for an additional 12 hours following the initial spin-up time. The various error statistics computed are defined as follows.

Root-mean-square error (rmse)

$$\text{rmse} = \left[1/n \sum_{i=1}^{n} (\Delta H_i)^2 \right]^{1/2} \tag{20a}$$

Mean absolute error (MAE)

$$\text{MAE} = 1/n \sum |\Delta H_i| \tag{20b}$$

Mean error (bias) $\Delta\bar{H}$

$$\Delta\bar{H} = 1/n \sum \Delta H_i \tag{20c}$$

TABLE 3*a*. Model Wave Height Root-Mean-Square Error Based on a Total of 69 Grid Points Located Mainly Over Deep Waters for Each of 13 Six-Hourly Map Times

	September 9–13, 1978					September 16–19, 1978				
Day	Hour, UT	SASS	Ship	Mixed	Blended	Day	Hour, UT	SASS	Ship	Mixed	Blended
Sept. 10	0000	1.35	1.50	1.46	1.48	Sept. 16	1200	1.11	1.35	1.27	1.39
	0600	0.99	1.22	1.08	1.10		1800	0.91	1.06	0.99	1.10
	1200	1.05	1.33	1.17	1.10	Sept. 17	0000	0.83	0.93	0.86	0.98
	1800	1.37	1.50	1.30	1.35		0600	0.70	0.84	0.72	0.86
Sept. 11	0000	1.63	1.74	1.68	1.69		1200	0.72	0.87	0.76	0.87
	0600	1.20	1.61	1.28	1.38		1800	0.61	0.83	0.71	0.78
	1200	1.25	1.44	1.43	1.39	Sept. 18	0000	0.83	0.93	0.93	0.97
	1800	1.23	1.17	1.07	1.12		0600	0.86	1.04	0.94	1.06
Sept. 12	0000	1.60	1.22	1.36	1.37		1200	1.02	1.16	1.11	1.22
	0600	1.46	1.19	1.24	1.22		1800	0.94	1.23	1.01	1.18
	1200	1.29	1.52	1.30	1.18	Sept. 19	0000	1.04	1.30	1.17	1.28
	1800	1.20	1.63	1.52	1.05		0600	0.97	1.39	1.04	1.19
Sept. 13	0000	1.30	1.62	1.35	1.13		1200	1.22	1.48	1.24	1.39

The daily rmse values (in meters) are tabulated for each of the two periods using four different wind specifications after the model is driven for an additional 12 hours following the initial spin-up time of 24 hours. The wave height error, ΔH = model SWH − METOC SWH.

Scatter index (SI)

$$\text{SI} = \text{rmse}/\bar{H}_0 \tag{20d}$$

Correlation coefficient r

$$r = \left(1/n \sum H_i H_{0i} - \bar{H}\bar{H}_0 \right) / (s_h s_{0h}) \tag{20e}$$

In the above, $\Delta H_i = H_i - H_{0i}$ is the wave height error defined as model SWH minus observed SWH, where observed refers to either METOC wave height or altimeter wave height; $\bar{H}_0$ and $\bar{H}$ are the means of H_{0i} and H_i, respectively, s_{0h} and s_h the corresponding standard deviations, and n the total number of data points.

The various error parameters defined in (20) are displayed in Tables 3*a* and 3*b*. A detailed discussion and a quantitative evaluation of these error parameters are deferred until the following section. For a qualitative evaluation, the rmse at each grid point is computed using the height differences for the 13 six-hourly map times, and the spatial distributions of the rmse fields generated using four different wind specifications are presented in Figures 11*a*–11*d*. These figures show that the rmse tends to be generally large south of the QE2 storm track in the areas of highest sea states. Although relatively large, the SASS, mixed, and blended SWH errors are lower than the ship SWH error as demonstrated by the larger area enclosed by the 2-m rmse isopleth in Figure 11*b*. This area is smallest for the SASS rmse in Figure 11*a*, while the corresponding areas for the mixed rmse in Figure 11*c* and blended rmse in Figure 11*d* reflect the larger error contribution to the rmse field from the ship winds.

4.2. *Hindcast Period September 16–19, 1978*

For this period, wave generation was less active than that found in the first period but Seasat altimeter wave data were available for validation. On September 16 a low-pressure area occupied eastern Canada, a frontal trough with a series of low-pressure centers stretched across the southeastern section of the study area, and a ridge of high pressure was sandwiched between the low in the northwest and the trough in the southeast. In the area northeast of Newfoundland, a flow of 10–15 m/s, mainly from south to southwest, persisted for most of the period, becoming weaker by September 19. By September 18 tropical storm Hope was moving into the area from the southwest. Both Hope and the low over eastern Canada moved northeastward, giving a large low-pressure area over the western North Atlantic on September 18. By 1200 UT on September 19, Hope became part of an extratropical depression centered near 41°N/38°W with a central pressure ~986 mbar, while the northern low filled to ≈1004 mbar from an initial central pressure of 986 mbar, thus providing a weaker pressure gradient in the northwestern section. The wave heights based on METOC analyses were generally under 6 m at the beginning of the period. By 1200 UT on September 17, heights greater than 6 m accom-

TABLE 3*b*. Same as Table 3*a* but the Statistics Are Based on 897 Values by Combining the Individual Map Times to Produce a Mean Value for Each of the Two Periods

	September 9–13, 1978				September 16–19, 1978			
	SASS	Ship	Mixed	Blended	SASS	Ship	Mixed	Blended
rmse, m	1.31	1.45	1.33	1.29	0.92	1.13	1.00	1.11
MAE, m	1.05	1.12	1.04	1.01	0.72	0.89	0.79	0.90
Bias, m	−0.05	−0.32	−0.30	−0.34	−0.51	−0.85	−0.67	−0.83
SI, %	29	32	29	28	35	43	38	42
r, %	70	73	74	74	61	60	62	62

The table includes other error parameters, namely, MAE, bias, SI, and r as defined in (20).

panying tropical storm hope were analyzed as the storm propagating from the southwest was absorbed into the extratropical depression on September 19.

As previously described, rmse values at each grid point are calculated from the wave height fields generated at each of the 13 map times for the period 1200 UT on September 16 to 1200 UT on September 19. The spatial distributions of the rmse fields for the four different wind inputs are presented in Figures 12*a*–12*d*. In general, smaller values of rmse are observed in the area northeast of Newfoundland, where the wind forcing was relatively steady with long fetch and duration. Higher values of rmse are found in the southeast in the vicinity of the track of tropical storm Hope and in the area of general frontal troughing. Here, the wind forcing undergoes larger fluctuations in the areas of highest sea states, producing relatively larger wave height errors. The area enclosed by the 1.5-m rmse isopleth in Figure 12*b* is larger than the corresponding areas in Figures 12*a*, 12*c*, and 12*d*. This lends further support to the supposition that the model hindcasts of SWH are improved when SASS winds are assimilated into the wind forcing.

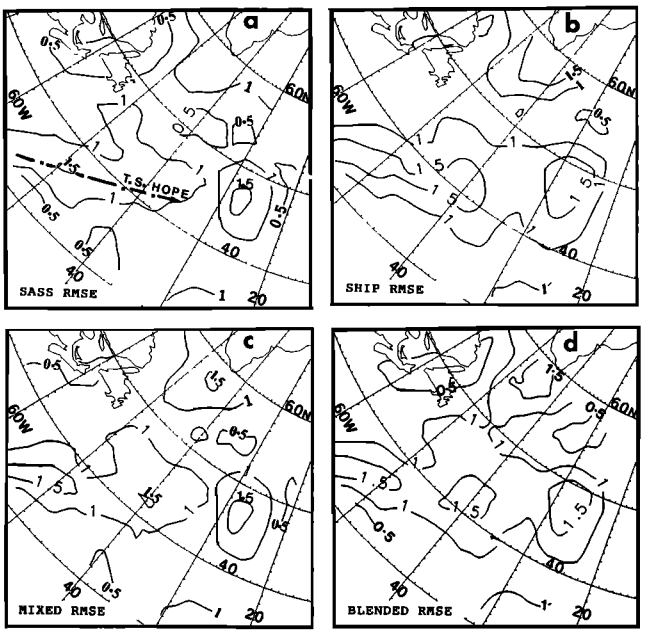

Fig. 12. Spatial distributions of root-mean-square height error (model SWH minus METOC SWH) in meters for the model output period 1200 UT on September 16, 1978, to 1200 UT on September 19, 1978, based on (*a*) SASS winds, (*b*) ship winds, (*c*) mixed winds, and (*d*) blended winds. The track of tropical storm Hope is shown by the dash-dot line in Figure 12*a*.

4.3. *A Quantitative Evaluation*

The various wave error statistics defined in (20) are obtained for each of the two periods, and the results are presented in Tables 3*a* and 3*b* for the four different wind inputs. In Table 3*a* the rmse values are given for individual map times covering the two periods. For each map time the rmse is based on 69 grid points located mainly over deep-water regions of the grid. In Table 3*b* the error statistics for the individual map times are combined and presented for each of the two periods. Besides rmse values, Table 3*b* includes other error parameters, namely, MAE, bias, scatter index, and linear correlation coefficient. The rmse values for individual analysis times fluctuate from one map time to the next. However, there is a definite trend toward lower rmse values associated with the SASS or mixed wind fields as against those obtained using ship-only winds, and this trend is evident in both periods. The daily rmse values are indicative of the order of magnitude of errors to be expected in the mean and are comparable with those obtained by *Pickett et al.* [1986].

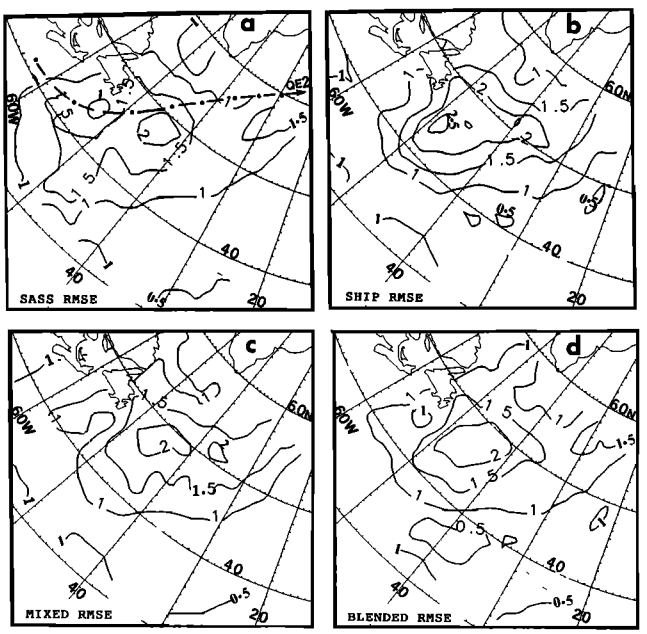

Fig. 11. Spatial distributions of root-mean-square height error (model SWH minus METOC SWH) in meters for model output period 0000 UT on September 10, 1978 to 0000 UT on September 13, 1978, based on (*a*) SASS winds, (*b*) ship winds, (*c*) mixed winds, and (*d*) blended winds. The track of the QE2 storm is shown by the dash-dot line in Figure 11*a*.

It can be seen in Table 3*b* that in the mean the rmse values of the model wave heights are reduced when the wind specification includes the SASS winds. For the two periods, a reduction of up to 18% in the rmse of the wave heights generated by the ship-only winds is realized, while the scatter index shows a reduction of 3–8%. The various models used by Pickett referred to earlier produced scatter indexes ranging from 30% to 80%. In this study the Resio model produces scatter indexes varying from 29% to 43% and therefore shows a high degree of skill. An examination of the bias indicates that the Resio model, in general, underestimates the wave heights, but it is less biased when the SASS and mixed wind fields are used as inputs.

During the period September 16–19, 1978, the Seasat radar altimeter was functioning and provided wave height data along the tracks. These wave data constitute the second comparison data set and are identified as the altimeter SWH and denoted by H_A. They are used here to evaluate the model-generated SWH interpolated to the altimeter SWH points as described in section 2. The validation is made for Seasat passes 1165 at 1110 UT and 1166 at 1250 UT on September 16, 1174 at 0240 UT on September 17, 1194 at 1155 UT on September 18, and 1208 at 1125 UT and 1209 at 1300 UT on September 19. These orbits are within ±3 hours of the analysis times 0000 and 1200 UT in open waters over

TABLE 4. Evaluation of Model SWH Against the Seasat Altimeter SWH Along the Satellite Tracks 1165, 1166, 1174, 1194, 1208, and 1209 for the Period September 16–19, 1978

Model Wind Input	SWH Error Statistics				
	rmse, m	MAE, m	Bias, m	SI, %	r, %
SASS	0.51	0.41	−0.05	25	73
Ship	0.68	0.52	−0.33	33	61
Mixed	0.62	0.48	−0.23	30	63
Blended	0.65	0.50	−0.31	31	69

The wave error parameters of rmse, bias, SI, and r as defined in (20) are tabulated for four different wind specifications. The statistics are based on a combined total of 497 data points for the six orbits. The wave height error ΔH = model SWH − altimeter SWH.

the northwest Atlantic and lie in well-defined pressure and flow fields. Orbits near the boundaries of the analysis area and in weak pressure gradient field are omitted. Wave height error statistics for the different wind specifications are obtained using (20), in which $n = 497$ is the total number of data points for the six orbits, and the results are presented in Table 4.

An examination of Table 4 shows that the SASS-derived wave heights provide the best error statistics in terms of the lowest rmse and highest correlation coefficient. Wave error statistics based only on ship winds are the poorest. The rmse of the wave heights (generated by the ship-only winds) is reduced by 25% when the wind input based only on SASS winds is used, while the reduction is up to 9% when a mixed or a blended wind field is used. A similar reduction is seen in respect to MAE and the scatter index. The linear correlation coefficient between model and altimeter wave heights shows a significant increase with SASS-only winds, while a moderate increase is realized with a blended or a mixed wind field. The model wave heights, in general, are underestimated, with the smallest bias associated with the SASS SWH.

Figure 13 is an example of plots of model-generated, altimeter, and METOC wave heights along orbit 1174 around analysis time 0000 UT on September 17. The altimeter heights are sampled at more frequent spatial intervals and show more variability along the track, while the model and METOC heights at the corresponding altimeter locations are based on a weighted average of the four grid point values surrounding each altimeter location and are therefore smoother. The METOC heights are, in general, larger than the altimeter heights but maintain nearly the same spatial trend. This feature is also exhibited for the other five satellite tracks. The altimeter data are considered to be nearer to the true wave height data; hence the rmse values of Table 4 are smaller than those of Table 3. Since the Resio model underestimates the wave heights in both periods when either the METOC or the altimeter data is used as the comparison data, the reduction in the rmse with the inclusion of SASS winds is in the right direction, that is, toward the true wave data.

5. Conclusions

The present study emphasizes the data preparation and the integration of the remotely sensed SASS winds with the conventional ship winds to produce wind fields suitable for driving a spectral ocean wave model. The model results are validated against ship and remotely sensed wave data to provide an assessment of the impact of SASS winds on ocean wave analysis and modeling. The important findings of this study are as follows.

1. The integration of SASS winds with the conventional ship winds provides an improved description of the synoptic wind field as revealed by the QE2 storm of September 9–12, 1978.

2. An analysis of wave height errors reveals that the assimilation of the dealiased SASS winds into the wind analyses generates wave height fields that are more accurate than the wave fields generated by using only the ship winds. For the two data analysis periods used in this study, the integration of SASS winds provides a reduction in the root-mean-square wave height errors of up to 25% as estimated by the Seasat altimeter.

3. Wave height contour and error analyses of the blended SWH and the mixed SWH suggest that the analyzed wind field created by merging the data sets is a better approach of integrating the SASS winds with the ship winds than the approach of weighting the gridded SASS winds with the gridded ship winds.

4. The inclusion of SASS winds in the wind inputs to the wave model produces a positive impact on the significant wave height field, irrespective of whether the comparison data are based on the METOC wave charts or the altimeter wave data.

This study suggests the feasibility of using scatterometer winds in operational wave analysis and modeling. With improved communications technology and objective dealiasing methods, it is possible to include scatterometer winds in an operational environment. The European Space Agency ERS-1 satellite, scheduled to be launched in late 1990, is expected to provide dealiased radar scatterometer winds and radar altimeter wave height data within 3 hours of the satellite observation. This raises the possibility of using the scatterometer wind data for creating more accurate wind

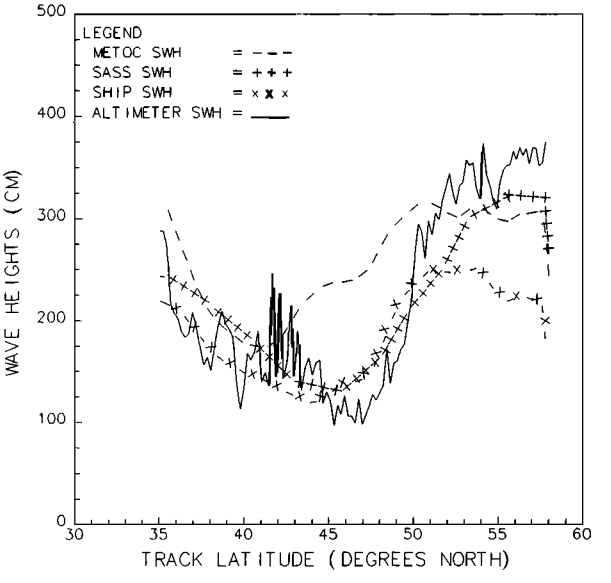

Fig. 13. Plots of altimeter SWH, METOC SWH, and model-generated SASS SWH (based on only SASS winds) and ship SWH (based on only ship winds) as a function of latitude along orbit 1174 at around 0000 UT on September 17, 1978.

fields and the altimeter wave data for generating initial sea states to improve ocean wave nowcasting and forecasting.

Acknowledgments. The authors gratefully acknowledge the valuable computer support provided by Norbert Driedger, Hao Le, and John A. Lewis of the Aerospace Meteorology Division, Atmospheric Environment Service (AES). Special thanks are due to V. Swail and R. D. Brown of the Canadian Climate Centre, AES, for making available the Geostrophic Wind Climatology data, to the Meteorology and Oceanography Centre, Halifax, Department of National Defence, for the operationally produced wave height charts, and to the Marine Environmental Data Service, Department of Fisheries and Oceans, for the Seasat altimeter wave data. Finally, the authors wish to extend their appreciation to the reviewers, whose comments have resulted in an improved version of this paper.

REFERENCES

Anthes, R. A., Y.-H. Kuo, and J. R. Gyakum, Numerical simulations of a case of explosive marine cyclogenesis, *Mon. Weather Rev., 111*, 1174–1188, 1983.

Aune, R. M., and T. T. Warner, Impact of Seasat wind data on a statistically initialized numerical model, paper presented at the Sixth Conference on Numerical Weather Prediction, Am. Meteorol. Soc., Omaha, Nebr., 1983.

Baker, W. E., R. Atlas, E. Kalnay, M. Halem, P. M. Woiceshyn, S. Peteherych, and D. Edelman, Large-scale analysis and forecast experiments with wind data from Seasat A scatterometer, *J. Geophys. Res., 89*, 4927–4936, 1984.

Benjamin, S. G., and N. L. Seaman, Objective analysis in curved flow, paper presented at the Sixth Conference on Numerical Weather Prediction, Am. Meteorol. Soc., Omaha, Nebr., 1983.

Bergman, K. H., and W. D. Bonner, Analysis error as a function of observation density for satellite temperature soundings with spatially correlated errors, *Mon. Weather Rev., 104*, 1308–1316, 1976.

Brown, R. D., and V. R. Swail, Spatial correlation of marine wind speed observations, *Atmos. Ocean, 26*, 524–540, 1988.

Cardone, V. J., Potential impact of remote sensing data on sea-state analysis and prediction, Oceanweather Inc. final report, 95 pp., Goddard Space Flight Cent., Greenbelt, Md., 1983.

Cressman, G. P., An operational objective analysis system, *Mon. Weather Rev., 87*, 367–374, 1959.

Duffy, D., and R. Atlas, The impact of Seasat A scatterometer data on the numerical prediction of the Queen Elizabeth II storm, *J. Geophys. Res., 91*, 2241–2248, 1986.

Duffy, D., R. Atlas, T. Rosmond, E. Baker, and R. Rosenberg, The impact of Seasat scatterometer winds on the Navy's operational model, *J. Geophys. Res., 89*, 7238–7244, 1984.

Inman, R. L., Operational objective analysis schemes at the National Severe Storms Forecast Center, *Natl. Severe Storms Lab. Tech. Cir. 10*, 50 pp., Environ. Sci. Serv. Admin., Norman, Okla., 1970.

Jet Propulsion Laboratory, Seasat Gulf of Alaska Workshop II report, Calif. Inst. of Technol., Pasadena, 1980.

Jones, W. L., L. C. Schroeder, D. H. Boggs, E. M. Bracalente, R. A. Brown, G. J. Dome, W. J. Pierson, and F. J. Wentz, The Seasat A satellite scatterometer: The geophysical evaluation of remotely sensed wind vectors over the ocean, *J. Geophys. Res., 87*, 3297–3317, 1982.

Khandekar, M. L., B. M. Eid, and V. Cardone, An intercomparison study of ocean wave models during the Canadian Atlantic Storms Program—Some preliminary results, *Rep. Ser. 065*, Environ. Stud. Revolving Funds, Ottawa, Canada, 1986.

Lalbeharry, R., Application of Seasat scatterometer winds for ocean wave analysis and modeling, *Atmos. Res. Dir. Rep. MSRB-88-3*, 98 pp., Atmos. Environ. Serv., Downsview, Ont., Canada, 1988.

Low, T. B., and V. R. Swail, Suitability of offshore hindcast surface winds for climatological applications, in *Proceedings, International Workshop on Offshore Winds and Icing*, edited by T. A. Agnew and V. R. Swail, Atmospheric Environment Service, Downsview, Ont., Canada, 1985.

Morgan, M. R., The analysis and forecasting of sea and swell conditions in open water, *Tech. Memo. TEC 763*, 32 pp., Atmos. Environ. Serv., Ont., Canada, 1971.

Offiler, D., Surface wind vector measurements from satellites, in *Proceedings of the NATO Advanced Study Institute on Remote Sensing Applications in Marine Science and Technology*, edited by A. P. Cracknell, pp. 169–182, D. Reidel, Hingham, Mass., 1982.

Penicka, F. X., Wave hindcast sensitivity, *Rep. Ser. 065*, Environ. Stud. Revolving Funds, Ottawa, Canada, 1986.

Peteherych, S., M. G. Wurtele, P. M. Woiceshyn, D. H. Boggs, and R. Atlas, First global analysis of Seasat scatterometer winds and potential for meteorological research, paper presented at the Symposium on Frontiers of Remote Sensing of the Oceans and Troposphere from Air and Space Platforms, Union Radio Sci. Int., Shoresh, Israel, May 14–23, 1984.

Peteherych, S., W. S. Appleby, P. M. Woiceshyn, J. C. Spagnol, and L. Chu, Application of Seasat scatterometer wind measurements for operational short-range weather forecasting, *Weather Forecasting, 3*, 89–103, 1988.

Pickett, R. L., D. L. Burns, and R. D. Broome, Comparison of wind and wave models with GEOSAT, *Rep. 201*, 8 pp., U.S. Nav. Ocean Res. and Dev. Activity, Natl. Space Technol. Lab., Miss., 1986.

Queffeulou, P., Seasat wave height measurement: A comparison with sea-truth data and wave forecasting model: Application to the geographic distribution of strong sea states in storms, *J. Geophys. Res., 88*, 1779–1788, 1983.

Resio, D. T., Estimation of wind-wave generation in a discrete spectral model, *J. Phys. Oceanogr., 11*, 510–525, 1981.

Resio, D. T., An assessment of wave hindcast methodologies in the Scotian Shelf, Grand Banks, and Labrador Sea areas, *Can. Contr. Rep. Hydrogr. Ocean Sci. 4*, 128 pp., Dep. of Fish. and Oceans, Ottawa, Ont., Canada, 1982.

Schroeder, L. C., D. H. Boggs, G. Dome, I. M. Halberstam, W. L. Jones, W. J. Pierson, and F. J. Wentz, The relationship between wind vector and normalized radar cross section used to derive Seasat A satellite scatterometer winds, *J. Geophys. Res., 87*, 3318–3336, 1982.

Seaman, R. S., Objective analysis of statistical interpolation and successive correction schemes, paper presented at the Sixth Conference on Numerical Weather Prediction, Am. Meteorol. Soc., Omaha, Nebr., 1983.

Stephens, J. J., and J. M. Stitt, Optimum influence radii for interpolation with the method of successive corrections, *Mon. Weather Rev., 98*, 680–687, 1970.

Swail, V. R., Geostrophic wind climatology of Canadian marine areas, *CCC Rep. 85-9*, 94 pp., Atmos. Environ. Serv., Downsview, Ont., Canada, 1985.

Wurtele, M. G., P. M. Woiceshyn, S. Peteherych, M. Barowski, and W. S. Appleby, Wind direction removal studies of Seasat scatterometer derived winds, *J. Geophys. Res., 87*, 3365–3377, 1982.

Yu, T. W., and R. D. McPherson, Global data assimilation experiments with scatterometer winds from Seasat A, *Mon. Weather Rev., 112*, 368–376, 1984.

M. L. Khandekar, R. Lalbeharry, and S. Peteherych, Meteorological Services Research Branch, Atmospheric Environment Service, 4905 Dufferin Street, Downsview, Ontario, Canada M3H 5T4.

(Received February 17, 1989;
accepted June 22, 1989.)